PNAS RESEARCH ARTICLE | EARTH, ATMOSPHERIC, AND PLANETARY SCIENCES

Rate of atmospheric brown carbon whitening governed by environmental conditions

Elijah G. Schnitzler[a,1], Nealan G. A. Gerrebos[b,1], Therese S. Carter[c], Yuanzhou Huang[b], Colette L. Heald[c,d,2], Allan K. Bertram[b,2], and Jonathan P. D. Abbatt[e,2]

Edited by Akkihebbal Ravishankara, Colorado State University, Fort Collins, CO; received March 30, 2022; accepted August 2, 2022

Biomass burning organic aerosol (BBOA) in the atmosphere contains many compounds that absorb solar radiation, called brown carbon (BrC). While BBOA is in the atmosphere, BrC can undergo reactions with oxidants such as ozone which decrease absorbance, or whiten. The effect of temperature and relative humidity (RH) on whitening has not been well constrained, leading to uncertainties when predicting the direct radiative effect of BrC on climate. Using an aerosol flow-tube reactor, we show that the whitening of BBOA by oxidation with ozone is strongly dependent on RH and temperature. Using a poke-flow technique, we show that the viscosity of BBOA also depends strongly on these conditions. The measured whitening rate of BrC is described well with the viscosity data, assuming that the whitening is due to oxidation occurring in the bulk of the BBOA, within a thin shell beneath the surface. Using our combined datasets, we developed a kinetic model of this whitening process, and we show that the lifetime of BrC is 1 d or less below ∼1 km in altitude in the atmosphere but is often much longer than 1 d above this altitude. Including this altitude dependence of the whitening rate in a chemical transport model causes a large change in the predicted warming effect of BBOA on climate. Overall, the results illustrate that RH and temperature need to be considered to understand the role of BBOA in the atmosphere.

biomass burning | organic aerosol | brown carbon | multiphase chemistry | aerosol kinetics

Significance

Biomass burning organic aerosol (BBOA) has a significant direct effect on climate by absorbing solar radiation. Understanding this effect is increasingly important as wildfires become more prevalent in several regions across the globe. While transported in the atmosphere, BBOA can react with atmospheric oxidants, leading to less-absorbing products, or whitening. We show that this whitening is strongly influenced by relative humidity and temperature and, consequently, vertical transport in the atmosphere. Implementing altitude-dependent whitening of BBOA in a global atmospheric model indicates that the effects of changing environmental conditions need to be included when simulating the direct climate effects of BBOA.

Biomass burning is a significant source of organic aerosol to the atmosphere, and the mass of this aerosol is expected to increase in the future as forest fires increase in occurrence across diverse regions due to climate change (1, 2). Biomass burning organic aerosol (BBOA) contains a significant amount of light-absorbing material, referred to as brown carbon (BrC). This light-absorbing material exerts a positive radiative effect on Earth's climate, leading to a strong warming effect, dictated in part by its lifetime in the atmosphere (3–5).

In the atmosphere, BrC is susceptible to a wide range of chemical aging processes, in addition to dilution (6, 7), such as photolysis and heterogeneous oxidation with OH, O_3, and NO_3, which alter its light-absorption properties (8–13). After an initial period when darkening may occur (13, 14), steady whitening (i.e., decreasing absorbance) of BrC occurs for some conditions found in the troposphere (15–18). For example, in two studies, the light absorption of BrC was observed to decrease exponentially with transport time with a timescale of about 1 d (15, 19), and this evolution is associated with changes in composition, including an increase in the oxidation level of BBOA (15, 20) and the degradation of small chromophores (21, 22), like nitrophenols (23, 24). On the other hand, for BrC in a convection outflow at high altitude, no whitening was observed after 1 d of subsequent aging (25).

Heat from biomass burning sources can enhance vertical transport by convection and result in the formation of pyrocumulus and pyrocumulonimbus clouds (26, 27), such that BrC from wildfires can be transported to the middle and upper troposphere and even the lower stratosphere (25, 28–30). As BBOA is transported vertically, it is exposed to rapidly changing environmental conditions, signified by the lapse rate of -6.5 K km^{-1}. Relative humidity (RH) also fluctuates with altitude, although not uniformly. Overall, the effect of RH and temperature on the lifetime of BrC is poorly constrained, leading to uncertainty when predicting the radiative effect of BrC on climate. The phase state of organic aerosol is strongly dependent on temperature and RH (31–34). Secondary organic aerosol (SOA) in particular is modeled to be in a glassy state across the globe at altitudes greater than 5 km (35, 36), and primary BBOA will likely respond similarly to the rapidly changing environmental conditions upon vertical transport. If BBOA is solid or highly viscous, slow diffusion of organic species and oxidants within the particles will limit reactivity (37, 38). If BrC is long-lived in the middle and upper troposphere, then its overall radiative effect may be larger than previously expected (39, 40).

Author contributions: E.G.S., C.L.H., A.K.B., and J.P.D.A. designed research; E.G.S., N.G.A.G., T.S.C., and Y.H. performed research; E.G.S., N.G.A.G., T.S.C., and Y.H. analyzed data; and E.G.S., N.G.A.G., T.S.C., Y.H., C.L.H., A.K.B., and J.P.D.A. wrote the paper.

The authors declare no competing interest.

This article is a PNAS Direct Submission.

[1]E.G.S. and N.G.A.G. contributed equally to this work.

[2]To whom correspondence may be addressed. Email: heald@mit.edu or bertram@chem.ubc.ca or jonathan.abbatt@utoronto.ca.

This article contains supporting information online at http://www.pnas.org/lookup/suppl/doi:10.1073/pnas.2205610119/-/DCSupplemental.

Published September 12, 2022.

Here, we report complementary laboratory experiments, kinetic simulations, and global model simulations to determine the effect of RH and temperature on the time scales for whitening of BrC by heterogeneous reaction with ozone throughout the troposphere and to assess the impact of BrC on Earth's radiative balance. Water-soluble BBOA samples were generated by controlled smoldering of wood. The whitening of the BrC component was investigated across a range of RH and temperature conditions relevant to the free troposphere, from the planetary boundary layer (PBL) at about 1 km to the tropopause, using a cooled flow tube, in which RH was precisely controlled down to 253 K. The viscosity of the BBOA was investigated across a range of RH conditions using the poke-flow technique (41), and the viscosity measurements were used to develop a parameterization of viscosity as a function of RH and temperature. Based on this parameterization, kinetic simulations of the experimental data provide insights into the mechanism of the reaction, and they inform global chemical transport model simulations that were performed to assess the direct radiative effect (DRE) of BrC on climate.

Results and Discussion

Whitening of BrC as a Function of RH and Temperature. BBOA contains a wide range of phenolic molecules, originating from the thermal degradation of lignin, including species such as sinapaldehyde and coniferaldehyde (42, 43). These representative species with exocyclic carbon-carbon double bonds are reactive with ozone (44, 45) and exhibit marked visible-light absorption (43). To determine the reactivity of BrC with ozone, laboratory-generated pine BBOA was extracted into water and aerosolized, and the resulting submicron particles, with a geometric mean diameter of about 100 nm, were exposed to ozone in a reaction flow tube, equipped with precise RH and temperature control, as shown in *SI Appendix*, Fig. S1 (see *Materials and Methods*).

The metric used for reactivity was relative absorption at 405 nm, measured for suspended particles downstream of the flow tube using a photoacoustic spectrometer. Relative absorption was quantified by comparing measurements of the absorption coefficient at 405 nm when ozone was present to those when ozone was absent. A representative time series of the absorption coefficient at 405 nm, shown in *SI Appendix*, Fig. S2, at 273 K and 20, 40, and 60% RH depicts the appreciable and variable extent of whitening that occurred due to exposure to ozone. In contrast to the absorption coefficient, the size distribution did not change upon ozone exposure (e.g., *SI Appendix*, Fig. S3). Throughout the flow-tube experiments, there was no evidence of particle growth or volatilization. Consequently, the observed decay in relative absorption was due to changes in the composition and absorptivity of the water-soluble BBOA, rather than changes in the particle size.

To compare whitening across a broad range of temperature and RH conditions, the relative absorption remaining after exposure to a high mixing ratio of ozone, 45 ppm, was measured at 253–293 K and 5–80% RH, with a fixed aerosol residence time of 130 s. The results of these experiments are summarized in Fig. 1*A*. For all temperatures, a strong dependence on RH was observed, with the amount of whitening decreasing with RH. For example, at 293 K, the absorption decreases by more than 40% at 60% RH but less than 5% at 5% RH. The amount of whitening was also strongly dependent on temperature. For example, at 60% RH, the extent of whitening went from more than 40% at 293 K to about 30% at 273 K and less than 10% at 253 K. Furthermore, at the lowest temperature, 253 K, and RH values less than or equal to 40%, the extent of whitening was too small to detect in our experiment, illustrating that whitening time scales can be long at low temperature and low RH.

Relative absorption as a function of ozone mixing ratio was also measured for two temperatures and two relative humidities, yielding the results shown in Fig. 1*B*. At the given temperature and RH values, the relative absorption decreased as the ozone mixing ratio increased from roughly 5–45 ppm. At low ozone mixing ratios, there is no indication of absorption enhancement due to oxidation, associated with a relative absorption greater than one, so heterogeneous ozone oxidation led only to the whitening of the water-soluble BBOA considered here. Previously, exposure of BBOA extracts from the same source to aqueous OH radicals in bulk solutions led to an initial absorption enhancement at 400 nm, followed by slower, steady whitening (46). Similarly, exposure of whole suspended BBOA from the same source to gas-phase OH radicals led to absorption enhancement followed by whitening (8). On the other hand, exposure of whole suspended and filter-deposited BBOA from other sources

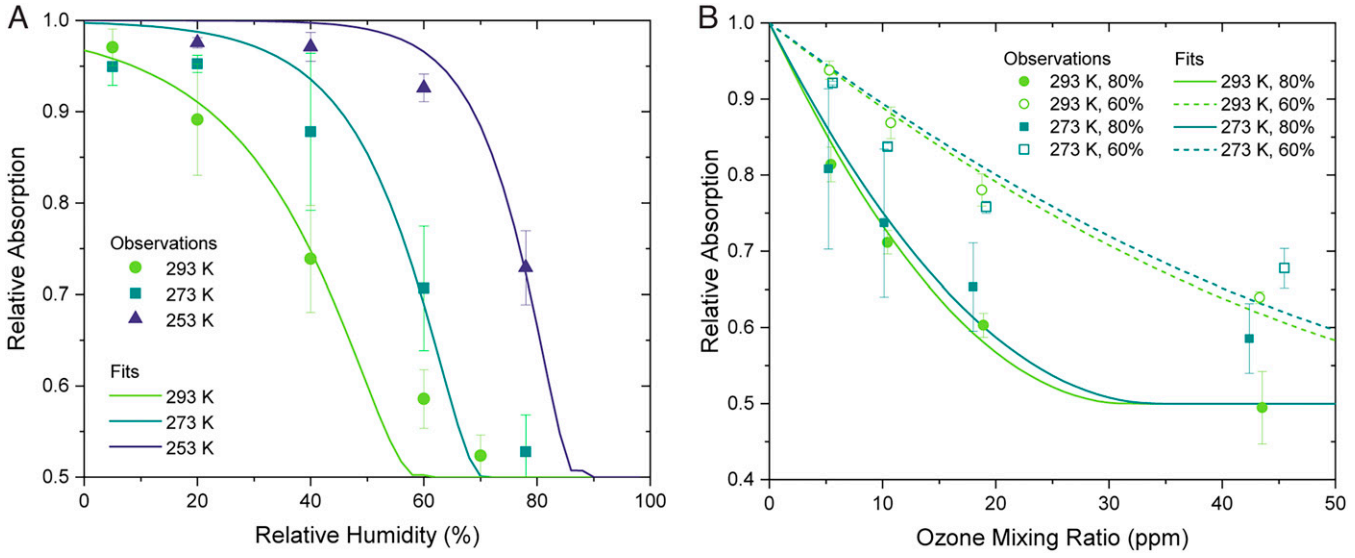

Fig. 1. Relative absorption at 405 nm remaining (*A*) after exposure to 45 ppm of ozone as a function of RH at 253, 273, and 293 K and (*B*) as a function of ozone mixing ratio at either 273 or 293 K and 60 or 80% RH. The curves represent fits of Eq. **2** to the experimental data points. Error bars represent one SD of four sets of datapoints.

to gas-phase ozone led only to whitening (9, 47), as observed here. Together, these observations suggest that the distinct optical evolution due to ozone relates to the identity of the oxidant rather than the composition of the BBOA in which the reaction occurs. The light-absorbing molecules that react with ozone may include sinapaldehyde, coniferaldehyde, and larger species with exocyclic carbon-carbon double bonds, which will be fragmented by the addition of ozone across the double bond. Electron-rich aromatic rings may also be reactive to ozone. Since whitening is observed without an accompanying change in particle size, the mass fraction of these species may be small, although they contribute a significant fraction of the total absorption.

The effects of RH and temperature, in addition to ozone mixing ratio, are also evident in Fig. 1*B*. Most apparent, the decay in the relative absorption was much faster at 80% RH than at 60% RH. At 293 K, the relative absorption reached an asymptote of 50% of the initial absorption at an ozone mixing ratio of 45 ppm, above which no additional whitening is expected. At 273 K, the relative absorption was still decreasing at 45 ppm, approaching the same asymptote. Previously, studies have suggested that a significant fraction of the light-absorbing species in whole BBOA from pine needle litter was either unreactive with ozone or physically protected from ozone at room temperature and 30% RH (9). The asymptote here similarly reflects the water-soluble BBOA constituents that are recalcitrant with respect to ozone, which account for 50% of the initial absorption.

Viscosity of BBOA as a Function of RH and Temperature. Reaction rates between organic aerosol constituents and gas-phase oxidants, including ozone, are governed in part by the viscosity of the particles (48). Viscosities of the water-soluble BBOA considered here were measured using the poke-flow technique (see *Materials and Methods*), allowing estimates of diffusion coefficients within the water-soluble BBOA and, in turn, insights into the reaction rates between BrC and ozone in the atmosphere and in the laboratory (i.e., flow-tube) experiments. Micrographs from poke-flow measurements for filter-collected BBOA extracted into water are shown in *SI Appendix*, Fig. S4. Experiments were performed at 294 K and 0–25% RH, and images from representative experiments at 0 and 25% RH are presented. Before being poked with a needle, the droplets were spherical in shape. Upon being poked, they adopted a half-torus geometry. With the needle removed, the droplets began to flow in order to decrease their surface energy, with a characteristic experimental recovery time, $\tau_{exp,\ flow}$. The experimental recovery time decreased significantly as RH increased, such that it was on the order of 1,000 s at 0% RH and 10 s at 25% RH, as shown in *SI Appendix*, Fig. S5.

The viscosities determined from these experimental flow times using fluid dynamic simulations are shown in Fig. 2*A*. The viscosity of the samples at 0% RH was $\sim 1–2 \times 10^5$ Pa s. For reference, the viscosity of peanut butter is $\sim 1 \times 10^3$ Pa s, and the viscosity of tar pitch is $\sim 1 \times 10^8$ Pa s (34). As the RH increased from 0 to 25%, the viscosity decreased by approximately a factor of 100. A decrease in viscosity with an increase in RH is expected since the water content of the BBOA is expected to increase, and water is known to be a plasticizer (i.e., the presence of water leads to a decrease in viscosity in highly viscous material (34)).

The viscosity data above were used to develop a parameterization of viscosity as a function of temperature and RH for BBOA (*SI Appendix*, section S1). The parameterization applies a mole-fraction-based Arrhenius mixing rule to describe viscosity as a function of RH and the Vogel-Folcher-Tamman equation to describe viscosity as a function of temperature, as has been done previously (35, 36, 49). The viscosity as a function of RH and temperature determined with this procedure is shown in Fig. 2*B*. Similar to the whitening experiments, a strong dependence on both RH and temperature is observed.

Analysis of BrC Whitening Kinetics Using the Viscosity Parameterization. The rate of whitening of BrC within the BBOA particles by ozone can be limited by several processes, including surface and bulk reaction rates between reactive BrC and ozone, solubility of ozone within the particles, and diffusion of ozone and BrC within the particles. The resistor model is a simple way to understand and account for these processes. If the reaction between ozone and BrC is fast and occurs in a

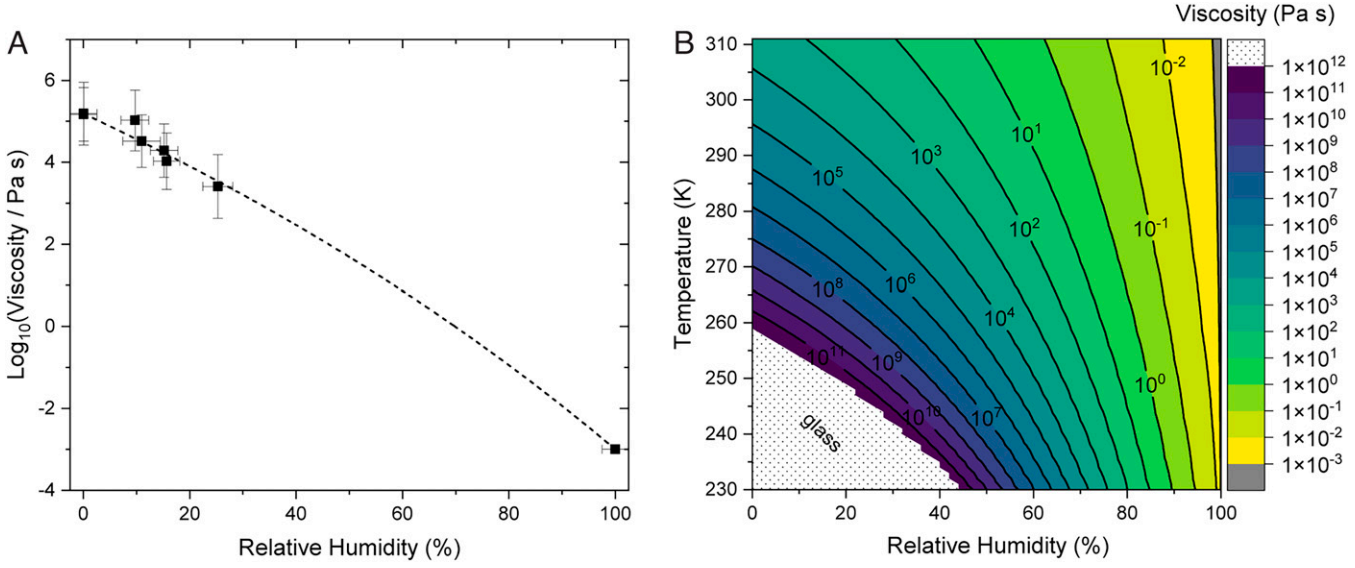

Fig. 2. Panel (*A*) shows viscosities of the BBOA as a function of RH. Symbols show the averages of the log(viscosity) values, with *y*-error bars representing the upper and lower limits at each RH and *x*-error bars representing the uncertainty in RH. Data for both 10 mL and 50 mL water extracts are shown (*SI Appendix*, Fig. S6). Included at RH of 100% is the viscosity of pure water at a temperature of 294 K. The black dashed curve corresponds to a fit to the data using the parameterization (*SI Appendix*, section S1). Panel (*B*) shows predicted viscosities of BBOA as a function of temperature and RH. Viscosities above 10^{12} Pa s correspond to a glass state and are cut off (dotted region) because they are not modeled well by the Vogel-Fulcher-Tamman equation.

thin layer near the surface, the reactivity of BrC within the particle can be described by the following equation based on the resistor model (50):

$$\sqrt{\frac{[\mathrm{BrC}](t)}{[\mathrm{BrC}]_0}} = 1 - \frac{3RTn_{\mathrm{O_3}(g)}H\sqrt{D_{\mathrm{O_3}}k_2}}{2a\sqrt{[\mathrm{BrC}]_0}}\,t \qquad [1]$$

where $[\mathrm{BrC}]_0$ is the initial concentration of BrC, R is the gas constant, T is the temperature, $n_{\mathrm{O_3}}$ is the concentration of ozone in the gas phase, H is Henry's law constant, $D_{\mathrm{O_3}}$ is the diffusion coefficient of ozone within the particles, k_2 is the second order rate coefficient for the ozonolysis of BrC within the particles, a is the radius of the aerosol particles, and t is the time. Eq. **1** assumes that BrC is uniform throughout the particles during ozonolysis. A time-scale analysis using estimated diffusion coefficients of BrC within the particles is consistent with this assumption (*SI Appendix*, section S2).

Eq. **1** can be rewritten in terms of ozone partial pressure, $P_{\mathrm{O_3}}$ (51), as shown in the *SI Appendix*, section S3. The fraction of BrC that remains unreacted was assumed to be equivalent to the absorption relative to the initial absorption, Abs_t/Abs_0. Furthermore, Abs_t/Abs_0 was forced to be ≥50% since the absorption of BrC never falls below ~50% of the initial value, regardless of RH or temperature (Fig. 1). Rearrangement of Eq. **1** and these constraints lead to the following equation:

$$\frac{Abs_t}{Abs_0} = 0.5\left(1 - \frac{3H\sqrt{D_{\mathrm{O_3}}k_2}}{2a\sqrt{[\mathrm{BrC}]_0}}P_{\mathrm{O_3}}t\right)^2 + 0.5 \qquad [2]$$

Eq. **2** was fit to the experimental measurements of relative absorption of BrC as a function of RH (Fig. 1*A*) and O_3 mixing ratio (Fig. 1*B*) to obtain $H(k_2/[\mathrm{BrC}]_0)^{1/2}$ at temperatures of 253, 273, and 293 K (*SI Appendix*, Fig. S7). For t and a, values of 130 s and 143 nm were used, based on the residence time and median volume radius of the particles used in the flow tube experiments. $D_{\mathrm{O_3}}$ was calculated using the parameterization for viscosity as a function of RH and temperature and the fractional Stokes-Einstein equation (52), as discussed in the *SI Appendix*, section S3. Shown in Fig. 1*A* are the fits of Eq. **2** to the experimental data for the unreacted BrC fraction as a function of RH at 293, 273, and 253 K. For these experiments, $P_{\mathrm{O_3}} = 4.5 \times 10^{-5}$ atm (45 ppm). Shown in Fig. 1*B* are the fits of Eq. **2** to the experimental data of Abs_t/Abs_0 as a function of O_3 mixing ratio at 293 and 273 K and 60 and 80% RH.

The good agreement between the experimental data and the fits to Eq. **2** in Fig. 1 is consistent with the reaction between O_3 and BrC occurring in the bulk of the BBOA, within a thin shell below the surface (50). Shown in *SI Appendix*, Fig. S7 are the $H(k_2/[\mathrm{BrC}]_0)^{1/2}$ values determined from the fits of Eq. **2** to the experimental data. There is not a strong dependence on temperature. A change in the reaction rate constant k_2 is expected, but it could be compensated for by a change in H. Furthermore, the $H(k_2/[\mathrm{BrC}]_0)^{1/2}$ values determined from the fits are consistent with values estimated based on literature data (*SI Appendix*, section S4). The line in *SI Appendix*, Fig. S7 represents a linear fit of the $H(k_2/[\mathrm{BrC}]_0)^{1/2}$ values as a function of temperature, and it was used when predicting the lifetime of BrC in the atmosphere, together with Eq. **1** (see below).

In addition to the analysis above, we also investigated if other model representations previously used to describe reactivity of particles were able to describe our experimental data well. For example, we compared the experimental data in Fig. 1*A* to predictions using the resistor model and assuming the reaction between O_3 and BrC was limited by only diffusion of BrC within the particles (*SI Appendix*, section S5). In this case, the agreement between the experimental data and the predictions was poor (*SI Appendix*, section S5). In addition, we considered the resistor model and assumed O_3 and BrC were well-mixed throughout the particles (*SI Appendix*, section S6). In this case, good agreement between the experimental data and model representation was only obtained if unrealistic values of H and k_2 are used (*SI Appendix*, section S6). We conclude that the model representation we used to describe our data (i.e., Eq. **1**) is a reasonable representation of our data since the data are described well by Eq. **1**, the $H(k_2/[\mathrm{BrC}]_0)^{1/2}$ values extracted from our fits are consistent with expectations, and two other model representations previously used to describe reactive uptake do not describe our data well.

Predictions of Lifetime and Direct Radiative Impacts of BrC in the Atmosphere. The lifetime of reactive BrC in the atmosphere due to this aging process influences its radiative effect and environmental impact. From Eq. **1**, the lifetime, τ_{BrC}, can be expressed as the following:

$$\tau_{\mathrm{BrC}} = \frac{\left(1 - \frac{1}{\sqrt{e}}\right)2a\sqrt{[\mathrm{BrC}]_0}}{3HP_{\mathrm{O_3}}\sqrt{D_{\mathrm{O_3}}k_2}} \qquad [3]$$

To calculate τ_{BrC} as a function of altitude and latitude in the atmosphere, first, annual average temperature and RH values as a function of altitude and latitude in the atmosphere were determined from MERRA2 data (40). Next, $D_{\mathrm{O_3}}$ as a function of altitude and latitude in the atmosphere was calculated using these temperature and RH fields, the fractional Stokes-Einstein equation, and our parameterization of viscosity as a function of temperature and RH (Fig. 2*B*). Finally, τ_{BrC} was calculated as a function of altitude and latitude using the $D_{\mathrm{O_3}}$ values as a function of altitude and latitude, the derived values for $H(k_2/[\mathrm{BrC}]_0)^{1/2}$ (line in *SI Appendix*, Fig. S7) and Eq. **3**. For the latter calculation, the following variables were used: $a = 150$ nm and $P_{\mathrm{O_3}} = 3.5 \times 10^{-8}$ atm, i.e., 35 ppb of ozone. The partial pressure of ozone was based on an average of measurements of tropospheric ozone at surface level and at 10 km, multiplied by the atmospheric pressures at the same altitudes (53–57). The radius was chosen based on volume size distributions of atmospheric BBOA (58–60). $H(k_2/[\mathrm{BrC}]_0)^{1/2}$ was calculated at each temperature using the fit in *SI Appendix*, Fig. S7, giving a value of ~9 $\mathrm{atm^{-1}\ s^{-1/2}}$ at all temperatures in the range evaluated.

Shown in Fig. 3*A* are the τ_{BrC} values as a function of altitude and latitude calculated with this approach, including the altitude corresponding to a τ_{BrC} of 1 d. The zonally averaged altitude for this lifetime is similar to the height of the PBL, i.e., very roughly 1 km. Throughout much of the mid- and upper troposphere, the whitening lifetime via this process is considerably longer than a typical particle residence time, which is often taken as roughly a week (61, 62). Indeed, for ozone, a fraction of the BBOA BrC was recalcitrant to whitening.

What is the impact of this altitude-dependent whitening process of BBOA BrC on its global concentration and DRE? To answer this question, a global three-dimensional chemical transport model, GEOS-Chem, was coupled to the RRTMG radiative transfer model (63) in a configuration known as GC-RT (64). The zonal concentration of BrC in the northern hemisphere (NH) and tropics is highest below 2.5 km, while in the southern hemisphere (SH), it is highest in the upper troposphere, as shown in Fig. 3*C*. As illustrated in Carter et al. (40), with no whitening included in the model, the global annual

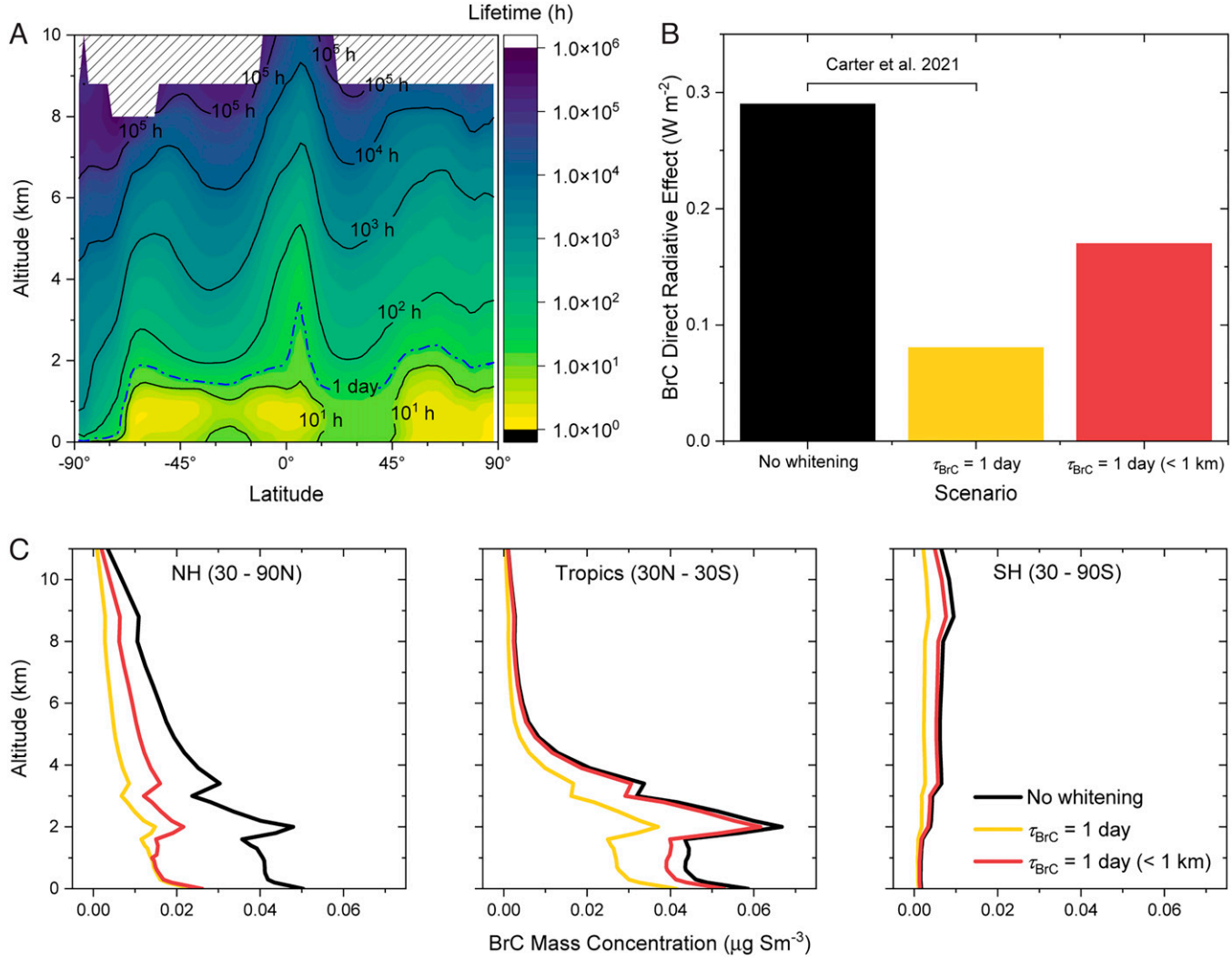

Fig. 3. Panel (*A*) shows the predicted annual average lifetimes of water-soluble BrC in the atmosphere as a function of altitude and latitude. The dashed blue line represents 1-d whitening of BrC. Panel (*B*) shows the global mean all-sky top-of-atmosphere BrC DRE in 2018 for the schemes with no-whitening, 1-d whitening, and 1-d whitening only below 1 km. The third scheme is new to this study; the first two schemes are described in Carter et al. (40). Panel (*C*) shows the simulated mean 2018 BrC mass concentrations by altitude for the northern hemisphere (30–90°N), the tropics (30°N–30°S), and the southern hemisphere (30–90°S) for the three schemes in panel (*B*). BrC mass concentrations are reported at standard conditions of temperature and pressure (STP: 273 K, 1 atm).

mean top-of-the-atmosphere DRE of BrC is 0.29 W m^{-2} and drops to 0.08 W m^{-2} when including whitening with a lifetime of 1 d at all altitudes (Fig. 3*B* and also see *SI Appendix*, Fig. S8).

When a whitening lifetime (of 1 d) is included only at altitudes below 1 km, in agreement with the current experimental results, the decrease in BrC concentration depends more strongly on region, with a significant decrease only in the NH (Fig. 3*C* and also see *SI Appendix*, Fig. S8). At high latitudes, where the PBL in fire regions is nearly always below 1 km, emitted BrC is efficiently whitened within the PBL, substantially decreasing BrC concentrations exported to the free troposphere. In the tropics, a deeper PBL allows BrC to be lofted above the whitening zone, leading to overall less efficient whitening. When limiting the whitening process to below 1 km, the decrease in the global DRE is less pronounced, reaching about 0.17 W m^{-2}, indicating that increased aerosol viscosity at high altitudes enhances the warming effect of BrC.

Atmospheric Implications. This work uniquely combines measurements of aerosol reactivity and viscosity with simulations of aerosol radiative effects to explore the critical impact of environmental conditions on the whitening of BrC BBOA and its DRE. Together, the results demonstrate that the timescale for whitening by ozone oxidation becomes longer than 1 d for altitudes greater than roughly 1 km. We stress that the specific timescale and altitude threshold for whitening will depend on a number of factors, including the size of the particles, environmental conditions, absorption wavelengths, and the concentrations and identity of the oxidants. In this work, heterogeneous oxidation by ozone of wood smoke was considered. Previous studies have shown that low temperatures can also reduce the rate of BBOA chemical aging by hydroxyl radicals (33, 65); although the direct connection to the optical properties of the particles was not made in those works. Low temperature NO_3 aging experiments have not yet been reported, nor have low temperature photoreaction studies of BBOA; although work using individual molecules (e.g., nitrophenols) has shown slower photodegradation rates in organic matrices (66). In addition, the nature of the BBOA BrC material should be varied in subsequent studies, to explore how this whitening phenomenon depends on composition, combustion conditions, and BrC water solubility.

Although the derived aging timescale of 24 h at about 1 km altitude in the atmosphere may vary somewhat as a function of environmental conditions, BBOA composition, and aging mechanism, the overall behavior demonstrated in this study is expected to be universal. In particular, it is expected that BrC aging processes will be slowest in regions of the atmosphere where the environmental conditions lead to high BBOA viscosity, such as the mid- and upper troposphere. As shown in this work, this will have significant effects on the DRE of BrC. Past models that have assumed a uniform BrC aging timescale of 1 d throughout the troposphere are likely underestimating the BrC DRE (39, 40). Indeed, we note that the environmental conditions in much of the mid- and upper troposphere lead to aging timescales of a week or more (Fig. 3*A*).

We finish by noting that the viscosity of BBOA may reach very high values, perhaps even those of a glass, under some environmental conditions such as those in the upper troposphere (Fig. 2*B* and see also *SI Appendix*, Fig. S9 for a global distribution of viscosity and glass state of BBOA). The rates of heterogeneous oxidation will be slower in more viscous particles, resulting in slower removal of the BBOA particles via wet deposition. As well, previous results have shown that certain types of glassy aerosol can act as ice nucleating particles and, hence, influence properties of clouds and climate (67, 68). Since BBOA may be in a glassy state in the upper troposphere, studies are needed to quantify the ice nucleation ability of glassy BBOA. Beyond effects on the DRE of BrC, which was the main focus of this paper, this may be another mechanism by which environmental conditions affect BBOA and its influence on climate.

Materials and Methods

BBOA Generation and Collection. Samples of BBOA were generated by controlled, low temperature smoldering of untreated, commercial pine wood in a heated flow tube (46, 69, 70). Clean air (Linde, Grade Zero 0.1) flowed through a quartz tube with an inner diameter of 2.2 cm at a rate of 2.0 L min^{-1}. A 30.5-cm length of the tube rested in a tube furnace (Thermo, Lindberg Blue M), and a 27.0-cm length extended downstream. Particles were collected on filters of borosilicate glass bonded to PTFE (Pall, Emfab).

For a typical sample of BBOA, three rectangular chips of pine, with a total mass of about 6 g, were placed in the quartz tube, and the furnace temperature was ramped to 673 K. Filter sampling began only after the wood had dried and once strong smoldering, with a distinct front, was observed; care was taken to avoid flaming conditions. For filter sampling, typically about 100 mg of whole BBOA was collected.

Heterogeneous Ozone Oxidation. It was important to prepare the sample flow with the correct RH at a specific temperature. To do this, the conditioned sample (*SI Appendix*, section S7) was directed into a double-jacketed glass flow tube, called the RH-conditioner, as in *SI Appendix*, Fig. S1. A recirculating chiller filled with a mixture of ethylene glycol and water was connected to flow through the inner jacket of this flow tube. RH was monitored at room temperature with a commercial probe (VWR). For experiments conducted at 253 and 273 K, ultrapure water was added to the conditioning flow tube, and its temperature was monitored continuously with a thermocouple. The sample in the RH-conditioner is assumed to be at ice saturation (71), and the temperature was adjusted such that the saturation vapor pressure of ice gave the desired RH once the sample was directed into the adjacent reaction flow tube, also double-jacketed.

Near the inlet of the reaction flow tube, ozone was added to the sample, in a carrier gas with a flow rate of 0.2 L min^{-1}, to give a total flow rate of 1.0 L min^{-1} through the flow tube. With the reaction volume, the residence time in the flow tube was 130 $\pm$ 10 s. The total aerosol mass loading in the flow tube was about 1,000 $\mu g\ m^{-3}$. Ozone was generated by passing clean, dry air (Linde, Grade Zero 0.1) through a small glass tube housing a Hg lamp at its center. The ozone mixing ratio was varied by adjusting the shielding around the Hg lamp and was measured for the same total flow rate using an ozone monitor (2B Technologies, 202). To allow as long a residence time as possible in the flow tube and still provide sufficient aerosol absorption, we did not monitor ozone continuously. A second recirculating chiller filled with the same ethylene-water mixture was connected to flow through the inner jacket of the reaction flow tube. The temperature was adjusted and monitored with a second thermocouple, which was retracted from the flow tube once the Hg lamp was turned on to introduce ozone. The RH in the reaction flow tube was calculated from its temperature and the water content of the sample leaving the RH conditioner.

Particle Viscosity Measurement. The viscosity of the aerosol particles nebulized and deposited on a hydrophobic glass slide was determined using the poke-flow technique (32, 41, 72). During the experiment, the slide and sample were placed inside a flow cell with both RH and temperature control. The sample was conditioned overnight (>12 h) at 294 $\pm$ 1 K, and the poke-flow measurement was performed at 2, 4, and 6 h after conditioning (within the uncertainties of the measurements, the viscosities did not depend on the conditioning time used, as shown in *SI Appendix*, Fig. S10). The glass slide was mounted in the flow cell with a hole at the top through which a needle could be inserted. The droplet was poked using a sharp needle (Ted Pella Company, 13561–20) coated with hydrophobic oil slip coating (Cytonix, OilSlip 110). The needle was attached to a micromanipulator stage, which allowed it to move in the *x*, *y*, and *z* directions.

In a typical experiment, the needle tip was aligned above the center of the droplet, and it was slowly lowered until it touched the particle and was then quickly raised, leaving a depression in the droplet and a shape similar to a half-torus geometry. The droplet began to flow to reduce its surface energy and eventually returned to the original spherical geometry. The change in morphology as a function of time was recorded with a CCD camera connected to a microscope (AmScope). The experimental flow (or recovery) time, $\tau_{exp,\ flow}$, was defined as the time taken for the equivalent area diameter of the hole to decrease to 50% of its original value. Fluid dynamic simulations were performed as discussed in the *SI Appendix*, section S8.

Global Transport and Radiative Transfer Modeling. The BrC simulation employed GEOS-Chem coupled to RRTMG (63) in a configuration known as GC-RT, v.12.3.0 (64), and was compared to previous results from Carter et al. (40). Simulations were performed at 2.0 $\times$ 2.5 degree horizontal resolution with 47 vertical levels and were driven by MERRA-2 meteorology. GFED4s was used to represent fire emissions. It was assumed that 100% of BBOA was brown or absorbing and that this was the only source of BrC. Details on BrC emissions and nonabsorbing organic aerosol optical properties used in the model are provided elsewhere (39, 73). The BrC absorption properties vary based on the BC-to-OA ratio (40), following Saleh, et al. (74). The lifetime for BrC whitening was treated as constant, set to 1 d. The whitening parameterization does not allow BrC absorptivity to drop below 25% of the starting value. The global whitening and nonwhitening simulations reported previously (40) are compared with the new simulation based on the laboratory results, in which whitening occurs only below 1 km.

Data, Materials, and Software Availability. All data in this article appear either in the main text or *SI Appendix*. Data will be shared upon request to one of the corresponding authors.

ACKNOWLEDGMENTS. This research was funded by the Natural Sciences and Engineering Research Council of Canada (NSERC). E.G.S. gratefully acknowledges a postdoctoral fellowship from NSERC. T.S.C. and C.L.H. acknowledge support from the U.S. National Science Foundation (NSF AGS 1936642).

Author affiliations: [a]Department of Chemistry, Oklahoma State University, Stillwater, OK 74078; [b]Department of Chemistry, University of British Columbia, Vancouver V6T 1Z1, Canada; [c]Civil and Environmental Engineering Department, Massachusetts Institute of Technology, Cambridge, MA 02139; [d]Earth, Atmospheric and Planetary Sciences, Massachusetts Institute of Technology, Cambridge, MA 02139; and [e]Department of Chemistry, University of Toronto, Toronto M5S 3H6, Canada

1. P. E. Dennison, S. C. Brewer, J. D. Arnold, M. A. Moritz, Large wildfire trends in the western United States, 1984–2011. *Geophys. Res. Lett.* **41**, 2928–2933 (2014).
2. J. G. Canadell *et al.*, Multi-decadal increase of forest burned area in Australia is linked to climate change. *Nat. Commun.* **12**, 6921 (2021).
3. R. Saleh, From measurements to models: Toward accurate representation of brown carbon in climate calculations. *Curr. Pollut. Rep.* **6**, 90–104 (2020).
4. C. E. Chung, V. Ramanathan, D. Decremer, Observationally constrained estimates of carbonaceous aerosol radiative forcing. *Proc. Natl. Acad. Sci. U.S.A.* **109**, 11624–11629 (2012).
5. H. Brown *et al.*, Biomass burning aerosols in most climate models are too absorbing. *Nat. Commun.* **12**, 277 (2021).
6. N. M. Donahue, A. L. Robinson, C. O. Stanier, S. N. Pandis, Coupled partitioning, dilution, and chemical aging of semivolatile organics. *Environ. Sci. Technol.* **40**, 2635–2643 (2006).
7. A. L. Hodshire *et al.*, Dilution impacts on smoke aging: Evidence in Biomass Burning Observation Project (BBOP) data. *Atmos. Chem. Phys.* **21**, 6839–6855 (2021).
8. E. G. Schnitzler, T. Liu, R. F. Hems, J. P. D. Abbatt, Emerging investigator series: Heterogeneous OH oxidation of primary brown carbon aerosol: Effects of relative humidity and volatility. *Environ. Sci. Process. Impacts* **22**, 2162–2171 (2020).
9. E. C. Browne *et al.*, Effect of heterogeneous oxidative aging on light absorption by biomass burning organic aerosol. *Aerosol Sci. Technol.* **53**, 663–674 (2019).
10. C. Li *et al.*, Formation of secondary brown carbon in biomass burning aerosol proxies through NO_3 radical reactions. *Environ. Sci. Technol.* **54**, 1395–1405 (2020).
11. B. J. Sumlin *et al.*, Atmospheric photooxidation diminishes light absorption by primary brown carbon aerosol from biomass burning. *Environ. Sci. Technol. Lett.* **4**, 540–545 (2017).
12. Z. Cheng *et al.*, Evolution of the light-absorption properties of combustion brown carbon aerosols following reaction with nitrate radicals. *Aerosol Sci. Technol.* **54**, 849–863 (2020).
13. J. P. S. Wong *et al.*, Atmospheric evolution of molecular-weight-separated brown carbon from biomass burning. *Atmos. Chem. Phys.* **19**, 7319–7334 (2019).
14. R. F. Hems, E. G. Schnitzler, C. Liu-Kang, C. D. Cappa, J. P. D. Abbatt, Aging of atmospheric brown carbon aerosol. *ACS Earth Space Chem.* **5**, 722–748 (2021).
15. H. Forrister *et al.*, Evolution of brown carbon in wildfire plumes. *Geophys. Res. Lett.* **42**, 4623–4630 (2015).
16. S. Dasari *et al.*, Photochemical degradation affects the light absorption of water-soluble brown carbon in the South Asian outflow. *Sci. Adv.* **5**, eaau8066 (2019).
17. Y. Chen *et al.*, Brown carbon in atmospheric fine particles in Yangzhou, China: Light absorption properties and source apportionment. *Atmos. Res.* **244**, 105028 (2020).
18. S. S. de Sá *et al.*, Contributions of biomass-burning, urban, and biogenic emissions to the concentrations and light-absorbing properties of particulate matter in central Amazonia during the dry season. *Atmos. Chem. Phys.* **19**, 7973–8001 (2019).
19. X. Wang *et al.*, Deriving brown carbon from multiwavelength absorption measurements: Method and application to AERONET and Aethalometer observations. *Atmos. Chem. Phys.* **16**, 12733–12752 (2016).
20. A. L. Hodshire *et al.*, Aging effects on biomass burning aerosol mass and composition: A critical review of field and laboratory studies. *Environ. Sci. Technol.* **53**, 10007–10022 (2019).
21. R. A. Di Lorenzo, C. J. Young, Size separation method for absorption characterization in brown carbon: Application to an aged biomass burning sample. *Geophys. Res. Lett.* **43**, 458–465 (2016).
22. R. A. Di Lorenzo *et al.*, Molecular-size-separated brown carbon absorption for biomass-burning aerosol at multiple field sites. *Environ. Sci. Technol.* **51**, 3128–3137 (2017).
23. R. Zhao *et al.*, Photochemical processing of aqueous atmospheric brown carbon. *Atmos. Chem. Phys.* **15**, 6087–6100 (2015).
24. R. F. Hems, J. P. D. Abbatt, Aqueous phase photo-oxidation of brown carbon nitrophenols: Reaction kinetics, mechanism, and evolution of light absorption. *ACS Earth Space Chem.* **2**, 225–234 (2018).
25. Y. Zhang *et al.*, Top-of-atmosphere radiative forcing affected by brown carbon in the upper troposphere. *Nat. Geosci.* **10**, 486–489 (2017).
26. N. P. Lareau, C. B. Clements, Environmental controls on pyrocumulus and pyrocumulonimbus initiation and development. *Atmos. Chem. Phys.* **16**, 4005–4022 (2016).
27. C. K. Gatebe, T. Varnai, R. Poudyal, C. Ichoku, M. D. King, Taking the pulse of pyrocumulus clouds. *Atmos. Environ.* **52**, 121–130 (2012).
28. F. Dahlkötter *et al.*, The Pagami Creek smoke plume after long-range transport to the upper troposphere over Europe–Aerosol properties and black carbon mixing state. *Atmos. Chem. Phys.* **14**, 6111–6137 (2014).
29. J. Ditas *et al.*, Strong impact of wildfires on the abundance and aging of black carbon in the lowermost stratosphere. *Proc. Natl. Acad. Sci. U.S.A.* **115**, E11595–E11603 (2018).
30. A. Ansmann *et al.*, Extreme levels of Canadian wildfire smoke in the stratosphere over central Europe on 21–22 August 2017. *Atmos. Chem. Phys.* **18**, 11831–11845 (2018).
31. S. S. Petters, S. M. Kreidenweis, A. P. Grieshop, P. J. Ziemann, M. D. Petters, Temperature- and humidity-dependent phase states of secondary organic aerosols. *Geophys. Res. Lett.* **46**, 1005–1013 (2019).
32. L. Renbaum-Wolff *et al.*, Viscosity of α-pinene secondary organic material and implications for particle growth and reactivity. *Proc. Natl. Acad. Sci. U.S.A.* **110**, 8014–8019 (2013).
33. J. Li, S. M. Forrester, D. A. Knopf, Heterogeneous oxidation of amorphous organic aerosol surrogates by O3, NO3, and OH at typical tropospheric temperatures. *Atmos. Chem. Phys.* **20**, 6055–6080 (2020).
34. T. Koop, J. Bookhold, M. Shiraiwa, U. Pöschl, Glass transition and phase state of organic compounds: Dependency on molecular properties and implications for secondary organic aerosols in the atmosphere. *Phys. Chem. Chem. Phys.* **13**, 19238–19255 (2011).
35. M. Shiraiwa *et al.*, Global distribution of particle phase state in atmospheric secondary organic aerosols. *Nat. Commun.* **8**, 15002 (2017).
36. A. M. Maclean *et al.*, Global distribution of the phase state and mixing times within secondary organic aerosol particles in the troposphere based on room-temperature viscosity measurements. *ACS Earth Space Chem.* **5**, 3458–3473 (2021).
37. T. Berkemeier *et al.*, Ozone uptake on glassy, semi-solid and liquid organic matter and the role of reactive oxygen intermediates in atmospheric aerosol chemistry. *Phys. Chem. Chem. Phys.* **18**, 12662–12674 (2016).
38. S. Zhou, M. Shiraiwa, R. D. McWhinney, U. Pöschl, J. P. D. Abbatt, Kinetic limitations in gas-particle reactions arising from slow diffusion in secondary organic aerosol. *Faraday Discuss.* **165**, 391–406 (2013).
39. X. Wang *et al.*, Exploring the observational constraints on the simulation of brown carbon. *Atmos. Chem. Phys.* **18**, 635–653 (2018).
40. T. S. Carter *et al.*, Investigating carbonaceous aerosol and its absorption properties from fires in the western United States (WE-CAN) and Southern Africa (ORACLES and CLARIFY). *J. Geophys. Res. Atmos.* **126**, e2021JD034984 (2021).
41. M. Song *et al.*, Relative humidity-dependent viscosities of isoprene-derived secondary organic material and atmospheric implications for isoprene-dominant forests. *Atmos. Chem. Phys.* **15**, 5145–5159 (2015).
42. J. J. Schauer, M. J. Kleeman, G. R. Cass, B. R. T. Simoneit, Measurement of emissions from air pollution sources. 3. C_1–C_{29} organic compounds from fireplace combustion of wood. *Environ. Sci. Technol.* **35**, 1716–1728 (2001).
43. L. T. Fleming *et al.*, Molecular composition and photochemical lifetimes of brown carbon chromophores in biomass burning organic aerosol. *Atmos. Chem. Phys.* **20**, 1105–1129 (2020).
44. S. Net, S. Gligorovski, S. Pietri, H. Wortham, Photoenhanced degradation of veratraldehyde upon the heterogeneous ozone reactions. *Phys. Chem. Chem. Phys.* **12**, 7603–7611 (2010).
45. S. Net, E. G. Alvarez, S. Gligorovski, H. Wortham, Heterogeneous reactions of ozone with methoxyphenols, in presence and absence of light. *Atmos. Environ.* **45**, 3007–3014 (2011).
46. R. F. Hems *et al.*, Aqueous photoreactions of wood smoke brown carbon. *ACS Earth Space Chem.* **4**, 1149–1160 (2020).
47. X. Fan *et al.*, The evolutionary behavior of chromophoric brown carbon during ozone aging of fine particles from biomass burning. *Atmos. Chem. Phys.* **20**, 4593–4605 (2020).
48. M. Shiraiwa, M. Ammann, T. Koop, U. Pöschl, Gas uptake and chemical aging of semisolid organic aerosol particles. *Proc. Natl. Acad. Sci. U.S.A.* **108**, 11003–11008 (2011).
49. A. M. Maclean *et al.*, Humidity-dependent viscosity of secondary organic aerosol from ozonolysis of β-caryophyllene: Measurements, predictions, and implications. *ACS Earth Space Chem.* **5**, 305–318 (2021).
50. D. R. Worsnop, J. W. Morris, Q. Shi, P. Davidovits, C. E. Kolb, A chemical kinetic model for reactive transformations of aerosol particles. *Geophys. Res. Lett.* **29**, 57–1–57-4 (2002).
51. J. W. Morris *et al.*, Kinetics of submicron oleic acid aerosols with ozone: A novel aerosol mass spectrometric technique. *Geophys. Res. Lett.* **29**, 71–1–71-4 (2002).
52. E. Evoy, S. Kamal, G. N. Patey, S. T. Martin, A. K. Bertram, Unified description of diffusion coefficients from small to large molecules in organic-water mixtures. *J. Phys. Chem. A* **124**, 2301–2308 (2020).
53. D. Tarasick *et al.*, Tropospheric Ozone Assessment Report: Tropospheric ozone from 1877 to 2016, observed levels, trends and uncertainties. *Elementa* **7**, 39 (2019).
54. A. S. Lefohn *et al.*, Tropospheric ozone assessment report: Global ozone metrics for climate change, human health, and crop/ecosystem research. *Elementa (Wash D C)* **6**, 27 (2018).
55. J. Staehelin, W. Schmid, Trend analysis of tropospheric ozone concentrations utilizing the 20-year data set of ozone balloon soundings over Payerne (Switzerland). *Atmos. Environ. A Gen. Topics* **25**, 1739–1749 (1991).
56. S. Park, S.-W. Son, M.-I. Jung, J. Park, S. S. Park, Evaluation of tropospheric ozone reanalyses with independent ozonesonde observations in East Asia. *Geosci. Lett.* **7**, 12 (2020).
57. S. Sandroni, D. Anfossi, Trend of Ozone in the free troposphere above Europe. *Il Nuovo Cimento C* **18**, 497–503 (1995).
58. S. Shi *et al.*, Biomass burning aerosol characteristics for different vegetation types in different aging periods. *Environ. Int.* **126**, 504–511 (2019).
59. X. Yu *et al.*, Aerosol optical properties during firework, biomass burning and dust episodes in Beijing. *Atmos. Environ.* **81**, 475–484 (2013).
60. K. O. Ogunjobi, Z. He, K. W. Kim, Y. J. Kim, Aerosol optical depth during episodes of Asian dust storms and biomass burning at Kwangju, South Korea. *Atmos. Environ.* **38**, 1313–1323 (2004).
61. C. Papastefanou, Residence time of tropospheric aerosols in association with radioactive nuclides. *Appl. Radiat. Isot.* **64**, 93–100 (2006).
62. T. Tokieda, K. Yamanaka, K. Harada, S. Tsunogai, Seasonal variations of residence time and upper atmospheric contribution of aerosols studied with Pb-210, Bi-210, Po-210 and Be-7. *Tellus B Chem. Phys. Meterol.* **48**, 690–702 (1996).
63. M. J. Iacono *et al.*, Radiative forcing by long-lived greenhouse gases: Calculations with the AER radiative transfer models. *J. Geophys. Res. Atmos.* **113**, D13103 (2008).
64. C. L. Heald *et al.*, Contrasting the direct radiative effect and direct radiative forcing of aerosols. *Atmos. Chem. Phys.* **14**, 5513–5527 (2014).
65. J. Li, D. A. Knopf, Representation of multiphase OH oxidation of amorphous organic aerosol for tropospheric conditions. *Environ. Sci. Technol.* **55**, 7266–7275 (2021).
66. M. L. Hinks *et al.*, Effect of viscosity on photodegradation rates in complex secondary organic aerosol materials. *Phys. Chem. Chem. Phys.* **18**, 8785–8793 (2016).
67. B. J. Murray *et al.*, Heterogeneous nucleation of ice particles on glassy aerosols under cirrus conditions. *Nat. Geosci.* **3**, 233–237 (2010).
68. M. J. Wolf *et al.*, A biogenic secondary organic aerosol source of cirrus ice nucleating particles. *Nat. Commun.* **11**, 4834 (2020).
69. A. Trofimova, R. F. Hems, T. Liu, J. P. D. Abbatt, E. G. Schnitzler, Contribution of charge-transfer complexes to absorptivity of primary brown carbon aerosol. *ACS Earth Space Chem.* **3**, 1393–1401 (2019).
70. E. Evoy *et al.*, Diffusion coefficients and mixing times of organic molecules in β-caryophyllene secondary organic aerosol (SOA) and biomass burning organic aerosol (BBOA). *ACS Earth Space Chem.* **5**, 3268–3278 (2021).
71. R. W. Hyland, A. Wexler, Formulation for the thermodynamic properties of the saturated phases of H_2O from 173.15 K to 473.15 K. *ASHRAE Trans.* **89**, 500–519 (1983).
72. J. W. Grayson, M. Song, M. Sellier, A. K. Bertram, Validation of the poke-flow technique combined with simulations of fluid flow for determining viscosities in samples with small volumes and high viscosities. *Atmos. Meas. Tech.* **8**, 2463–2472 (2015).
73. X. Wang *et al.*, Exploiting simultaneous observational constraints on mass and absorption to estimate the global direct radiative forcing of black carbon and brown carbon. *Atmos. Chem. Phys.* **14**, 10989–11010 (2014).
74. R. Saleh *et al.*, Brownness of organics in aerosols from biomass burning linked to their black carbon content. *Nat. Geosci.* **7**, 647–650 (2014).